MAGNETOHYDRODYNAMICS Vol. 59 (2023), No. 3-4, pp. 391–399
DOI: 10.22364/mhd.59.3-4.11

NUMERICAL STUDY OF HEATING AND MELTING OF METAL IN THE INDUSTRIAL SCALE DIRECT CURRENT ELECTRICAL ARC FURNACE

S. Pavlovs[1*], *A. Jakovičs*[1], *A. Chudnovsky*[2]

[1] *University of Latvia, 3 Jelgavas str., Riga, Latvia*
[*] *e-Mail: sergejs.pavlovs@lu.lv*
[2] *JSC LATVO, 53 Ganibu Dambis, Riga, Latvia*

The article deals with the study of the heating and melting process for the industrial scale direct current electrical arc furnace (DC EAF). Numerical modelling was performed using the enthalpy and porosity approach at equal values of metal solidus and liquidus temperatures when the mushy zone is represented by the linear distribution of the mass fraction. The heat flux supplied through the arc spot is estimated using the heat balance equation taking into account metal heating and melting, Joule heat, radiation at the metal mirror and convective heat transfer at the metal vessel covered with firebricks. Electrical parameters of the arc between the top electrode and the melt mirror are estimated using the heat flux value. Computed distributions of the metal liquid/solid mass fraction make it possible to estimate duration of heating and melting.

Introduction. Previous studies of the authors deal with numerical and experimental study of the electro-vortex flow (EVF) and temperature field in liquid metal in a vessel with DC power supply through a system of bifilar electrodes [1]. The developed and experimentally verified numerical approach [1] was applied to calculate the turbulent EVF of the melt, the homogenization process of the melt temperature and alloying additive concentration [2] in the industrial scale direct current electrical arc furnace (DC EAF).

Further development of the numerical approach [3] which is associated with the simulation of heating and melting of metal was approved for the industrial mini DC EAF (with a capacity of 4.6 kg of molten steel). The industrial mini furnace was developed, manufactured and installed at LATVO JSC (Riga, Latvia). Melt temperature measurements

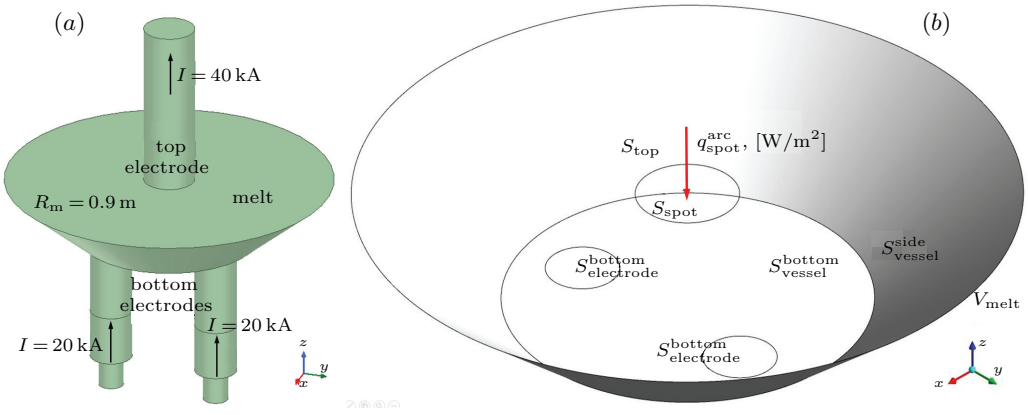

Fig. 1. Models of the industrial scale DC EAF for computations of (*a*) electromagnetic field; (*b*) solid/liquid metal temperature and melt EVF with Ansys Maxwell and Ansys Fluent, accordingly.

Table 1. Geometric parameters of melt, electrodes and parameters of supplied DC.

Melt vessel (truncated cone)	
Top (melt mirror) radius	$r_{\mathrm{m}}^{\mathrm{top}} = 0.9\,\mathrm{m}$
Bottom radius	$r_{\mathrm{m}}^{\mathrm{bottom}} = 0.5\,\mathrm{m}$
Height	$H_{\mathrm{m}} = 0.335\,\mathrm{m}$
Top electrode	
Arc spot radius at the melt mirror	$r_{\mathrm{el}}^{\mathrm{top}} = 0.14\,\mathrm{m}$
Bottom electrodes	
Radius of electrode without blades	$r_{\mathrm{el}}^{\mathrm{bottom}} = 0.115\,\mathrm{m}$
Distance between axes of electrodes	$L_{\mathrm{el-el}}^{\mathrm{bottom}} = 0.6\,\mathrm{m}$
Offset of electrode axes from the symmetry plane	$L_{\mathrm{shift}}^{\mathrm{bottom}} = 0.1\,\mathrm{m}$
Direct current (DC)	
Top electrode	$I_{\mathrm{el}}^{\mathrm{top}} = 40\,\mathrm{kA}$
Each of two bottom electrodes	$I_{\mathrm{el}}^{\mathrm{bottom}} = 20\,\mathrm{kA}$

Table 2. Physical parameters of electrodes, melt, and firebrick vessel.

Iron (Fe) melt	
Electrical conductivity	$\sigma_{\mathrm{m}} = 1.1{\cdot}10^{6}\ \mathrm{S/m}$
Density	$\rho_{\mathrm{m}} = 6.8{\cdot}10^{3}\ \mathrm{kg/m^3}$
Viscosity	$\eta_{\mathrm{m}} = 1.2{\cdot}10^{-3}\ \mathrm{kg/(m{\cdot}s)}$
Thermal expansion coefficient	$\beta \sim 9.9{\cdot}10^{-6}\ \mathrm{K^{-1}}$
Specific heat capacity	$c_{\mathrm{m}} = 775\ \mathrm{J/(kg{\cdot}K)}$
Thermal conductivity	$\lambda_{\mathrm{m}} = 33\ \mathrm{W/(m{\cdot}K)}$
Emissivity	$\varepsilon_{\mathrm{m}} = 0.5$
Melting point	$T_{\mathrm{melting}} = 1538.85\ ^{\circ}\mathrm{C}$
Latent heat of melting	$h_{\mathrm{melting}} = 2.471{\cdot}10^{5}\ \mathrm{J/kg}$
Boiling point	$T_{\mathrm{boiling}} = 2860.85\ ^{\circ}\mathrm{C}$
Latent heat of vaporization	$h_{\mathrm{vapor}} = 6.088{\cdot}10^{6}\ \mathrm{J/kg}$
Furnace cover	
Emissivity	$\varepsilon_{\mathrm{cover}} = 0.3$
Temperature	$T_{\mathrm{cover}} = 873\,\mathrm{K}$
Firebrick vessel	
Density	$\rho_{\mathrm{f}} = 1.8{\cdot}10^{3}\ \mathrm{kg/m^3}$
Specific heat capacity	$c_{\mathrm{f}} = 1250\ \mathrm{J/(kg{\cdot}K)}$
Thermal conductivity	$\lambda_{\mathrm{f}} = 0.5\ \mathrm{W/(m{\cdot}K)}$
Thickness	$d_{\mathrm{f}} = 0.25\,\mathrm{m}$
Convective heat transfer coefficient	$\alpha_{\mathrm{conv}} = 10\ \mathrm{W/(m^2{\cdot}K)}$
Graphite (C) top electrode	
Electrical conductivity	$\sigma_{\mathrm{e}}^{\mathrm{top}} = 7{\cdot}10^{4}\ \mathrm{S/m}$
Steel bottom electrodes	
Electrical conductivity	$\sigma_{\mathrm{e}}^{\mathrm{bottom}} \sim 1.1{\cdot}10^{6}\ \mathrm{S/m}$
Thermal conductivity	$\lambda_{\mathrm{e}} = 33\ \mathrm{W/(m{\cdot}K)}$

by a probe with a thermocouples sensor and an infra-red video camera and melt velocity estimations using snap-shots of particle motion over the melt mirror were made [3].

The current study deals with the simulation of heating and melting in the industrial scale DC EAF with a capacity of 3.6 tons of molten steel. The prototype is the DC EAF installed at the LATVO plant (see the photo and references in [2]).

The industrial scale DC EAF is shown schematically in Fig. 1*a* [2]. Geometric parameters of electrodes and supplied DC, of the melt and vessel as well as physical parameters of the melt, electrodes and vessel are collected in Tables 1, 2.

1. Numerical modelling of heating and melting processes.

The enthalpy (H) and porosity (Π) approach is used for modelling heating and melting processes which have been implemented in the Ansys Fluent commercial software package [4] based on the source papers [5, 6].

In order to track the melt interface, the liquid fraction ξ_l in every cell volume of the mesh in the metal domain is computed at each iteration taking into account the enthalpy balance. The liquid fraction indicates the fraction of the cell volume that is liquid. For the so-called mushy region, the value of the liquid fraction is $0 < \xi_\text{l} < 1$. The relationship between the liquid fraction ξ_l and the solid fraction ξ_s is

$$\xi_\text{l} = 1 - \xi_\text{s} \tag{1}$$

The mushy region with the partially molten material is considered as a pseudo-porous medium. The value of the porosity Π increases from $\Pi_\text{s} = 0$ for the solid phase to $\Pi_\text{l} = 1$ for the liquid phase as the material is melting: $\Pi_\text{s} = 0 < \Pi < 1 = \Pi_\text{l}$. The porosity and solid or liquid fraction relationship is the following: $\Pi = 1 - \xi_\text{s} = \xi_\text{l}$.

Hence, the velocity increases from $\mathbf{V} = \mathbf{V}_\text{s} = 0$ for the solid material in a cell when porosity is $\Pi_\text{s} = 0$ to the velocity value in a fully liquid cell $\mathbf{V} = \mathbf{V}_\text{l}$

$$\mathbf{V} = \begin{cases} \mathbf{V}_\text{l} & \text{for liquid phase,} \\ (1 - \xi_\text{s})\,\mathbf{V}_\text{l} = \xi_\text{l}\mathbf{V}_\text{l} & \text{for the mushy region,} \\ \mathbf{V}_\text{s} & \text{for solid phase.} \end{cases} \tag{2}$$

The enthalpy H of the material is defined as the sum of the sensible enthalpy h and the latent heat ΔH,

$$H = h + \Delta H, \quad h = h_\text{ref} + \int\limits_{T_\text{ref}}^{T} c_\text{p}\text{d}T \tag{3}$$

where h_ref is the reference enthalpy, T_ref is the reference temperature, c_p is the specific heat at constant pressure.

The latent heat ΔH is assumed as a function of the temperature T in the following form

$$\Delta H\,(T) = \begin{cases} \Delta H = h_\text{melting} & \text{for } T \geq T_\text{liquidus}, \\ [1 - \xi_\text{s}\,(T)]\,h_\text{melting} = \xi_\text{l}\,(T)\,h_\text{melting} & \text{for } T_\text{liquidus} > T \geq T_\text{solidus}, \\ 0 & \text{for } T < T_\text{solidus}, \end{cases} \tag{4}$$

where h_melting is the latent heat of the material.

To determine the evolution of the latent heat h_melting of the material in the mushy region, the relationship of the local solid fraction to the temperature T can be chosen

– for pure materials (for instance, fine metals), where phase changes occur at a distinct temperature, that is in the case of equal liquidus and solidus temperatures of the

melt, i.e. $T_{\text{liquidus}} = T_{\text{solidus}}$; the mushy zone is represented by the linear distribution of the mass fraction [5]:

$$\xi_{\text{s}}(T) = \begin{cases} 0 & \text{for } T \geq T_{\text{liquidus}}, \\ \dfrac{T_{\text{liquidus}} - T}{2T_{\text{liquidus}}} & \text{for } T_{\text{liquidus}} > T \geq T_{\text{solidus}}, \\ 1 & \text{for} T < T_{\text{solidus}}. \end{cases} \tag{5}$$

– for multi-component materials (for instance, alloys) when the phase change occurs over the temperature range, i.e. $T_{\text{liquidus}} \neq T_{\text{solidus}}$; the mass fraction in the mushy zone is represented by the expression [4, 6]:

$$\xi_{\text{s}}(T) = \begin{cases} 0 & \text{for } T \geq T_{\text{liquidus}}, \\ \dfrac{T_{\text{liquidus}} - T}{T_{\text{liquidus}} - T_{\text{solidus}}} & \text{for } T_{\text{liquidus}} > T \geq T_{\text{solidus}}, \\ 1 & \text{for} T < T_{\text{solidus}}. \end{cases} \tag{6}$$

with the necessity to apply more complicated equilibrium diagrams of the phase change.

2. Governing equations.

The governing equations – the energy equation (6), the momentum (7) and continuity (8) equations – for solving the melting problems can be written as

$$\frac{\partial(\rho H)}{\partial t} + \nabla(\rho H V) = \nabla(\lambda \nabla T) + \frac{|\mathbf{J}|^2}{\sigma} - \frac{\partial\left(\rho \overline{V'_i h'}\right)}{\partial x_i}, \tag{7}$$

$$\frac{\partial(\rho \mathbf{V})}{\partial t} + \frac{\partial(\rho V_i V_j)}{\partial x_j} = -\nabla p + \eta \Delta V + \rho \mathbf{g}(1 - \beta \Delta T) + \mathbf{J} \times \mathbf{B} + f_{\text{mush}} - \frac{\partial\left(\rho \overline{V'_i V'_j}\right)}{\partial x_j}, \tag{8}$$

$$\frac{\partial \rho}{\partial t} + \nabla(\rho \mathbf{V}) = 0. \tag{9}$$

Buoyancy, or the Archimedes force, is modelled with the Boussinesq approximation.

The physical fields and parameters in Eqs. (7)–(9) are the following: $\mathbf{V}$, p are the velocity and the pressure field in the melt; T is the temperature; $\mathbf{g}$ is the gravitational acceleration; $\mathbf{J}$ and $\mathbf{B}$ are the electrical current density and its self-magnetic field; η, ρ, β, λ, σ are, respectively, the dynamic viscosity, density, coefficient of thermal expansion, thermal conductivity, and electrical conductivity.

Note that the values of the listed above physical parameters are selected to correspond to the temperature of the molten metal and are considered constant in the calculation. At the next stage of research, calculations with temperature-dependent physical parameters are planned. In this case, an independent problem will be the formation of a table of values of physical parameters in a wide range of temperatures of the heated and melted metal. An additional difficulty will be solving Maxwell equations together with the transport equations for velocity and temperature.

In the momentum equation (8) in the mushy region, there is a momentum sink due to the decreased porosity, which is derived using the Kozeny–Carman equation [7, 8]:

$$\mathbf{f}_{\text{mush}} = -\frac{(1 - \xi_{\text{l}})^2}{\xi_{\text{l}}^3 + \epsilon} \mathbf{V} A_{\text{mush}}, \tag{10}$$

where $\mathbf{V}$ is the velocity of partly/fully liquid material, and A_{mush} is the mushy zone constant [kg/(m^{3}s)], which depends on the morphology of the partly liquid material in the mushy zone. The small number $\varepsilon = 0.001$ in Eq. (10) is introduced to prevent division by zero.

The vector of the turbulent enthalpy flux $\rho\overline{V'_i h'}$ and the tensor of turbulent (Reynolds) stresses $\rho\overline{V'_i V'_j}$ are modelled with the LES approach. Note that the sink, which is similar to Eq. (8) with the same constant, is added to all equations which describe the transport of turbulence.

The Lorentz force $\mathbf{J} \times \mathbf{B}$ in Eq. (8) and the Joule heat $|\mathbf{J}|^2/\sigma$ in Eq. (7) are the results of the calculations of the electromagnetic (EM) field which were performed using the Ansys Maxwell commercial software package for the model presented in Fig. 1*a* (see details in [2]). The electric arc at the boundary of the top graphite electrode with the melt mirror is not considered in the EM part of the problems. The heat flow from the arc spot is taken into account in the boundary condition when solving the thermal part of the problem. An estimation of the heat flux value is given in Eq. (11). The diameter of the arc spot is assumed to be equal to the diameter of the top electrode.

3. Boundary conditions.

The scheme of the industrial DC EAF for numerical modelling of the melt EVF and heating and melting processes is presented in Fig. 1*b*.

The boundary conditions for melt flow are the following:

• no-slip conditions at the surfaces of the vessel ($S^{\text{side}}_{\text{vessel}}$; $S^{\text{bottom}}_{\text{vessel}}$) and bottom electrodes ($S^{\text{bottom}}_{\text{electrode}}$) as well as at the liquid/solid boundaries in case of partly molten metal;

• free slip conditions at the melt mirror (S_{top}; S_{spot}) which is considered as the fix surface.

The boundary conditions for temperature are:

• the heat flux $q^{\text{arc}}_{\text{spot}}$ is supplied through the spot of the arc (S_{spot});

• the heat radiation from the top surface of the metal (S_{spot}) except for the arc spot zone;

• the convective heat transfer α_{conv} at the vessel ($S^{\text{side}}_{\text{vessel}}$; $S^{\text{bottom}}_{\text{vessel}}$) taking into account the thermal resistance of firebricks of thickness d_{f} (Table 2);

• the heat transfer through the bottom electrodes ($S^{\text{electrode}}_{\text{bottom}}$) from the melt to the cross-sections of electrodes which are not covered with firebricks.

4. Heat flux supplied through the arc spot in the industrial scale DC EAF.

The heat flux $q^{\text{arc}}_{\text{spot}}$ which is supplied through the spot of the arc (S_{spot}) at the melt mirror is estimated with the heat balance equation

$$
\begin{aligned}
q^{\text{arc}}_{\text{spot}} S_{\text{spot}} = {} & \frac{\sigma_{SB}\left(T^4_{\text{melting}} - T^4_{\text{cover}}\right) S_{\text{top}}}{1/\varepsilon_m + 1/\varepsilon_{\text{cover}} - 1} + \frac{\alpha_{\text{conv}}\lambda_f}{\lambda_f + \alpha_{\text{conv}} d_f}\left(T_{\text{melting}} - T_a\right) S_{\text{vessel}} \\
& + \frac{2\lambda_e}{d_f}\left(T_{\text{melting}} - T_{\text{cooling}}\right) S^{\text{bottom}}_{\text{electrode}} + \frac{c_m \rho_m V_{melt}\left(T_{\text{melting}} - T_{\text{initial}}\right)}{\Delta t} \\
& + \frac{h_{\text{melting}} V_{\text{melt}}}{\Delta t} - \int_{V_m} \frac{|\mathbf{J}|^2}{\sigma} \mathrm{d}V,
\end{aligned}
\tag{11}
$$

when the whole volume of liquid metal is at the temperature T_{melting}, c_m is the specific heat capacity. The right part of Eq. (11) contains the following terms:

• the heat radiation from the top surface (S_{top}) of the metal except for the arc spot zone (S_{spot}); the furnace has a cover with the emissivity $\varepsilon_{\text{cover}}$ and temperature T_{cover};

• the convective heat transfer with the coefficient α_{conv} at the metal vessel covered with firebricks ($S_{\text{vessel}} = S_{\text{vessel}}^{\text{side}} + S_{\text{vessel}}^{\text{bottom}}$) of thickness d_{f} (Table 2);

• the heat transfer through the bottom electrodes ($S_{\text{electrode}}^{\text{bottom}}$); the temperature of electrodes which are not covered with firebricks is the cooling temperature T_{cooling};

• the metal heating from the selected initial temperature T_{initial} till the melting temperature T_{melting} and then metal melting at T_{melting};

• the Joule heat source in the metal due to the electrical current density (J) which produces the self-magnetic field.

Eq. (11) includes the estimated time Δt of the melt heating and melting processes.

The estimated value $q_{\text{spot}}^{\text{arc}} \sim 5.1{\cdot}10^7\,\text{W/m}^2$ is obtained using the parameters from Tables 1, 2; the selected estimated time $\Delta t = 30\,\text{min}$ and $T_{\text{initial}} = T_a = 323.15\,\text{K}$.

According to the made estimations, the arc is the source of 99.8% of the heat supplied to the melt; the rest (0.2%) is the Joule heat in the metal. More than 89% of the supplied heat is necessary for metal heating (71.8%) and melting (17.2%).

Values of the voltage U_{arc} and resistance R_{arc} of the arc can be calculated from the estimated value of the heat $Q_{\text{arc}} = q_{\text{spot}}^{\text{arc}} S_{\text{spot}}$ supplied from the arc to the melt,

$$U_{\text{arc}} = \frac{Q_{\text{arc}}}{I_{\text{el}}^{\text{top}}}, \quad R_{\text{arc}} = \frac{U_{\text{arc}}}{I_{\text{el}}^{\text{top}}} \tag{12}$$

The estimated values are $U_{\text{arc}} \sim 78.2\,\text{V}$; $R_{\text{arc}} \sim 0.002\,\Omega$; the electrical power $P_{\text{arc}} \sim 3.1\,\text{MW}$.

5. Metal heating and melting in the industrial scale DC EAF.

Computational results for the heating and melting processes are obtained for fine iron ($T_{\text{melting}} = T_{\text{liquidus}} = T_{\text{solidus}}$) and for the mushy zone constant $A_{\text{mush}} \sim 10^3\,\text{kg/(m}^3\text{s)}$.

Fig. 2 shows the mass fraction of solid and liquid phases as a function of time. According to the computations, the total time of metal heating and melting considering

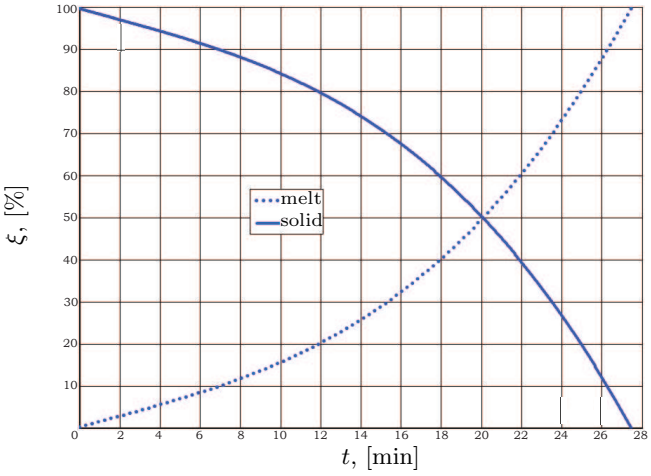

Fig. 2. Industrial scale DC EAF. Liquid ξ_{l} (dotted line) and solid ξ_{s} (solid line) mass fractions as a function of time t for the case $T_{\text{solidus}} = T_{\text{liquidus}}$, $A_{\text{mush}} = 10^3\,\text{kg/(m}^3{\cdot}\text{s)}$ – trend lines are shown.

turbulent EVF is $\Delta t = 27.5$ min. This value is very close to $\Delta t = 30$ min which was used for the estimation of the heat flux from the arc in Eq. (11) – the difference is $\sim 7.5\%$.

Fig. 2 illustrates the acceleration of the melting process due to the intensification of turbulent EVF in the increasing volume of the liquid phase: the first half of the metal volume was melt in 20 min, whereas the second half was melt in 7.5 min, or 2.66 times faster. Note that the acceleration of melting corresponds to the same parameter for the industrial mini industrial DC EAF [3].

The mass fraction of the liquid phase and the instantaneous velocity vectors for the melt EVF are illustrated in Figs. 3*a*,*c*,*e*,*g* for the cross-section $x = 0$ and in Figs. 3*b*,*d*,*f*,*h* for the cross-section $y = 0$. The flow time moments correspond to the parts [in %] of molten metal as selected from Fig. 2.

The instantaneous patterns of turbulent EVF at $x = 0$ (this vertical plane is parallel to a plane which includes both symmetry axes of the bottom electrodes) are approximately symmetrical about the z-axis. At the same time, the EVF patterns for $y = 0$ (this vertical plane is perpendicular to a plane, which includes both symmetry axes of two bottom electrodes) are not symmetrical about the z-axis since the Lorentz force near the bottom electrodes (see the offset of the electrodes axes from plane $x = 0$ in Table 1) confines the melt flow in the x-direction.

6. Unresolved problems of the computational model.

The distributions of instantaneous temperature in the melt near the central zone of the arc are not physically correct ($T > T_{\text{boiling}}$) because the Ansys Fluent module for the melting process computations does not cover the boiling phenomenon of liquid.

The volume with incorrect temperature values is relatively small if compare with the whole volume of the melt. Thus, the influence of the temperature distribution of this volume on the whole volume of the melt is vanishingly small.

Moreover, the ratio of the latent heat of vaporization to the latent heat of melting is $h_{\text{vapor}}/h_{\text{melting}} \sim 25$. Thus, we can conclude that this small region near the arc with non-physical temperature values will not exceed the limit.

Conclusions.

The obtained numerical results illustrate the dynamics of heating and melting processes as well as make possible estimations of the integral time of metal melting.

The reason for the acceleration of the melting process is the intensification of the developed turbulent electrovortex flow in a continuously increasing volume of molten metal.

The distribution of the liquid zone in the metal volume during melting is influenced by the molten metal flow structure, which depends on the position of bottom electrodes – the offset of the axes of the bottom electrodes from the symmetry plane in the industrial scale DC EAF results in the non-symmetry of the liquid zone. This effect was observed also in the industrial mini DC EAF [3].

Acknowledgements.

The European Regional Development Fund funded this study in the framework of the project "Development of Numerical Modelling Approaches to Study Complex Multiphysics Interactions in Electromagnetic Liquid Metal Technologies", contract no. 1.1.1.1/18/A/108.

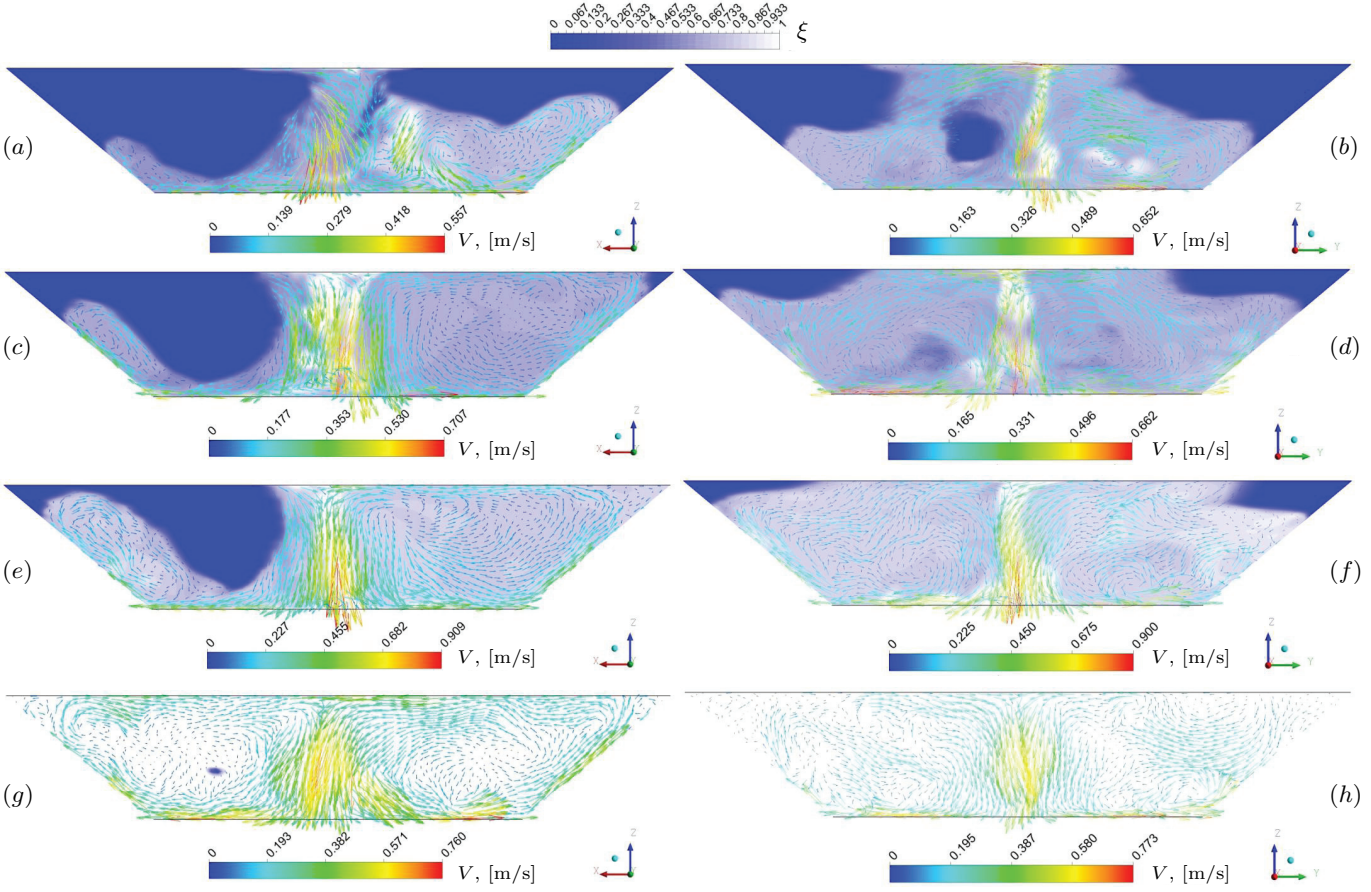

Fig. 3. Industrial scale DC EAF for the case $T_{\text{solidus}} = T_{\text{liquidus}}$, $A_{\text{mush}} = 10^3$ kg/(m^{3}s). Instantaneous distributions of mass fraction contours of solid/melt (blue/white) and melt velocity vectors in cross-sections: (a),(c),(e),(g) $x = 0$; (b),(d),(f),(h) $y = 0$: (a),(b) t = 845 s – 25% of melt; (c),(d) $t = 1220$ s – 50% of melt; (e),(f) $t = 1445$ s – 75% of melt; (g),(h) $t = 1675$ s – 100% of melt.

References

[1] S. Pavlovs, A. Jakovičs, A. Chudnovsky, Yu. Ivochkin, I. Teplyakov, D. Vinogradov. Numerical and experimental study of electrovortex flow and temperature field in liquid metal with bifilar power supply. *Magnetohydrodynamics*, vol. 58 (2022), no. 1–2, pp. 65–79; DOI: 10.22364/mhd.58.1-2.7.

[2] S. Pavlovs, A. Jakovičs, A. Chudnovsky. Electrovortex flow and melt homogenization in the industrial direct current electrical arc furnace. *Magnetohydrodynamic*, vol. 58 (2022), no. 3, pp. 305–326; DOI: 10.22364/mhd.58.3.7.

[3] S. Pavlovs, A. Jakovics, A. Chudnovsky. Heating and melting of metal in industrial mini direct current electrical arc furnace. *The International Journal for Computation and Mathematics in Electrical and Electronic Engineering (COMPEL)*, 2024; DOI: 10.1108/COMPEL-09-2023-0417 (in press).

[4] *Solidification and Melting. Chapter 18.* (ANSYS FLUENT Theory Guide. Release 14.5, October 2012), pp. 579–598.

[5] V.R. Voller, C. Prakash. A fixed grid numerical modelling methodology for convection-diffusion mushy region phase-change problems. *International Journal of Heat and Mass Transfer*, vol. 30 (1987), no. 8, pp. 1709–1719; DOI: 10.1016/0017-9310(87)90317-6.

[6] V.R. Voller, A.D. Brent, C. Prakash. Modelling the mushy region in a binary alloy. *Applied Mathematic Modelling*, vol. 14 (1990), no. 6, pp. 320–326; DOI: 10.1016/0307-904X(90)90084-I.

[7] J. Kozeny. Über kapillare Leitung des Wassers im Boden (Aufstieg, Versickerung und Anwendung auf die Bewässerung). *Sitzungsberichte der Akademie der Wissenschaften mathematisch-naturwissenschaftliche Klasse*, vol. 136-2a (1927) S. 271–306; https://www.zobodat.at/pdf/SBAWW_136_2a_0271-0306.pdf (in German).

[8] P.C. Carman. Fluid flow through granular beds. *Transaction of Institute of Chemical Engineers*, vol. 15 (1937), pp. 150–156; DOI: 10.1016/S0263-8762(97)80003-2.

Received 16.12.2023